

Evening out the spin and charge parity to increase T_c in unconventional superconductor Sr_2RuO_4

Swagata Acharya^{1*}, Dimitar Pashov¹, Cédric Weber¹,
Hyowon Park^{2,3}, Lorenzo Sponza⁴, Mark van Schilfgaarde¹

¹King's College London, The Strand, WC2R 2LS London, UK,

²Department of Physics, University of Illinois at Chicago, Chicago, Illinois 60607, USA,

³Materials Science Division, Argonne National Laboratory, Argonne, Illinois, 60439, USA,

⁴LEM UMR 104, ONERA-CNRS, F-92322, Châtillon, France

*E-mail: swagata.acharya@kcl.ac.uk.

Unconventional superconductivity in Sr_2RuO_4 has been intensively studied for decades. The origin and nature of the pairing continues to be widely debated, in particular, the possibility of a triplet origin of Cooper pairs. However, complexity of Sr_2RuO_4 with multiple low-energy scales, involving subtle interplay among spin, charge and orbital degrees of freedom, calls for advanced theoretical approaches which treat on equal footing all electronic effects. Here we develop a novel approach, a detailed *ab initio* theory, coupling quasiparticle self-consistent *GW* approximation with dynamical mean field theory (DMFT), including both local and non-local correlations. We report that the superconducting instability has multiple triplet and singlet components. In the unstrained case the triplet eigenvalues are larger than the singlets. Under uniaxial strain, the triplet eigenvalues drop rapidly and the singlet components increase. This is concomitant with our observation of spin and charge fluctu-

ations shifting closer to wave-vectors favoring singlet pairing in the Brillouin zone. We identify a complex mechanism where charge fluctuations and spin fluctuations co-operate in the even-parity channel under strain leading to increment in T_c , thus proposing a novel mechanism for pushing the frontier of T_c in unconventional ‘triplet’ superconductors.

Superconductivity (1) is a quantum phenomenon where electrons participate in dissipationless charge transport. While electrons repel each other via the Coulomb force, quantum theory provides additional interactions, that in special circumstances at low temperature, can overcome the repulsion to bind electrons in Cooper pairs (2). Within the paradigm of unconventional superconductivity the primary glue for the Cooper pairing can originate from collective bosonic excitations other than phonons. It usually involves spin fluctuations, but a general understanding of its origin is lacking. Here we focus on Sr_2RuO_4 (SRO), an unconventional superconductor which is highly sensitive to disorder (3). SRO is of great interest because there are indications that superconductivity has spin-triplet symmetry, which raises the possibility that it can sustain Majorana states conducive for topological quantum computing (4).

SRO single crystals were first shown to exhibit superconductivity below 1.5 K in 1994 (5); yet the origin for pairing is still debated (6). The superconducting transition temperature, T_c , has been observed to increase to 3 K in eutectic crystals of SRO, in the vicinity of Ru inclusions (7, 8, 9). While enhancement of T_c was traditionally associated with a reduced volume fraction, a recent series of experiments (10, 11) on bulk single crystals of SRO subject to uniaxial strain, show an increase to 3.4 K for compressive strain in the [100] direction, which we denote as ϵ_x . These apparently dissimilar studies hint towards a more common underlying mechanism for enhancement of T_c , since Ru inclusions induce local stresses which include uniaxial strain. In the tensile experiments T_c can be controlled by varying ϵ_x . It reaches a maximum value at $\epsilon_x=0.6\%$ (11), beyond which it falls rapidly. In what follows we will denote $\epsilon_x=0.6\%$ as ϵ_x^* .

These observations challenge the established belief that SRO is a spin-triplet (odd-parity) superconductor. Under strain, the tetragonal symmetry of the compound is lost, and it is no longer possible to find a triplet order parameter from two degenerate components, such as the usual p_x+ip_y or $d_{xz}+id_{yz}$. This raises the possibility for alternative mechanisms that could be responsible for pairing under strain.

The effect of strain on the Fermi surface has been studied with density functional theory (DFT) (11), and complementary minimal model Hamiltonian approaches (12, 13), which identified a change in Fermi surface topology. In particular, a Van Hove singularity (11) approaches the Fermi level, with a concomitant increase in charge carriers, which has been suggested as a possible mechanism for the increment in T_c (14) under strain. Such a picture identifies an important property resulting from strain, but it is not sufficient to explain the enhancement of T_c . In particular, the multi-orbital nature of the spin and charge fluctuations and many-body correlations are shown to be important in SRO (15, 16, 17, 18). Novel electron correlations originating from competition between non-local Coulomb repulsion and the large Hund's coupling (19, 15, 20) are also significant.

It is a formidable challenge to adequately describe the single- and two-particle responses needed for insights into the origin and nature of superconductivity in SRO. As we show here, an accurate theoretical formulation, that includes both local and non-local correlation effects in space, momentum and time and for all relevant degrees of freedom, is essential. Recently, a significant advance has been achieved by combining the quasi-particle self consistent GW (QSGW) approximation, with dynamical mean field theory (DMFT) (21, 22). Merging of these two state-of-the-art methods captures the effect of both strong local dynamic spin fluctuations (captured well in DMFT), and non-local dynamic correlation (23) effects (captured by QSGW), relying on neither model hamiltonians, nor on DFT, and avoiding the concomitant limitations they each carry. Also, nonlocal spin, charge and pairing susceptibilities can also be obtained

from vertices computed from the local two-particle Green's sampled by DMFT and bubble diagrams, via the solutions of Bethe Salpeter equations in respective channels. The full numerical implementation is discussed in Pashov et. al. (24) and codes are available on the open source electron structure suite Questaal (25).

Here we apply this new methodology to SRO, studying the pristine compound and also the effect of strain. Through the vertices and susceptibilities we can identify what drives superconductivity, and also what causes the non-monotonic dependence of T_c on strain. The pairing instability has multiple singlet and triplet components; nodal structure in singlet channel and nodeless odd-frequency structure in triplet channel. We find that the pairing is favored by even parity couplings in both spin and charge channels as ϵ_x approaches ϵ_x^* from below, while for $\epsilon_x > \epsilon_x^*$ incoherent spin fluctuations suppress the superconducting order. Our observations are in remarkable agreement with recent neutron scattering experiments (26).

Evolution of Fermi surface topology under strain: Fermi surfaces in the basal plane are shown in Fig. 1. The critical change in topology on the line connecting (0,0) and (0, π) (points Γ and M) occurs at $\epsilon_x=0.6\%$, in excellent agreement with ϵ_x^* . This is the strain where one Van-Hove singularity crosses E_F (see SM), as was noted in a prior DFT study; though in DFT it does so at a much larger ϵ_x (see Fig. 1). The Fermi surface generated by QSGW closely matches recent high-resolution bulk Fermi surface observed in quantum oscillation studies (27) angle-resolved photo-emission spectroscopy (28,29); indeed they can only be easily distinguished at higher resolution than Fig. 1 (as shown in SM, Fig. 1). That QSGW simultaneously yields the topology change close to the observed ϵ_x^* , and can reproduce fine details of the ARPES Fermi surface, is a reflection on its superior ability to generate good effective noninteracting Hamiltonians.

Spin fluctuations: incommensurability and coherence: Spin (χ^m) and charge (χ^d) susceptibilities are computed from momentum dependent Bethe-Salpeter equations 1 in magnetic (spin)

and density (charge) channels.

$$\chi_{\alpha_3, \alpha_4}^{m(d)}(i\nu, i\nu')_{\mathbf{q}, i\omega} = [(\chi^0)^{-1}_{\mathbf{q}, i\omega} - \Gamma_{loc}^{irr, m(d)}]_{\alpha_1, \alpha_2}^{-1}_{\alpha_3, \alpha_4}(i\nu, i\nu')_{\mathbf{q}, i\omega}. \quad (1)$$

χ^0 is the non-local (k -dependent) polarization bubble computed from single-particle QSGW Green's functions dressed by DMFT and Γ is the local irreducible two-particle vertex functions computed in magnetic and density channels. Γ is a function of two fermionic frequencies ν and ν' and the bosonic frequency ω . The susceptibilities $\chi^{m(d)}(\mathbf{q}, i\omega)$ are computed by closing $\chi_{\alpha_1, \alpha_2}^{m(d)}(i\nu, i\nu')_{\mathbf{q}, i\omega}$ with spin or charge bare vertex γ ($\gamma=1/2$ for spin and $\gamma=1$ for charge) and summing over frequencies ($i\nu, i\nu'$) and orbitals ($\alpha_{1,2}$) (see SM for derivations).

$$\chi^{m(d)}(\mathbf{q}, i\omega) = 2\gamma^2 \sum_{i\nu, i\nu'} \sum_{\alpha_1 \alpha_2} \chi_{\alpha_1, \alpha_2}^{m(d)}(i\nu, i\nu')_{\mathbf{q}, i\omega}. \quad (2)$$

We focus first on the Γ -X line of the Brillouin zone, where peaks appear in inelastic neutron scattering measurements (30, 31, 32) at the incommensurate vector $q^{IC}=(0.3, 0.3, 0)$ (in units $2\pi/a$) which a maximum in frequency near $\omega=10$ meV. Using DMFT, we compute $\chi^s(\mathbf{q}, \omega)$ by obtaining the local two-particle vertex in the spin channel and solving the Bethe-Salpeter equation (33), for varying amounts of strain. Consider first the unstrained case, when measurements are available. Fig. 2 shows $\chi^s(q, \omega)$ on the Γ -X line and in planes $q_z = 0, 1/4,$ and $1/2$ (in units of $2\pi/c$). The peak noted above [$q^{IC}=(0.3, 0.3, 0), \omega=10$ meV] is nearly independent of q_z , and moreover it disperses all the way up to 80 meV. All of these findings are in excellent agreement with experimental observations (34). We also find significant spin fluctuations at the ferromagnetic (FM) vector $q=(0, 0, 0)$ (also seen in very recent neutron measurements (26)) and almost no intensity at the antiferromagnetic nesting vector $(1/2, 1/2, 0)$. The FM signal is important, because of its implications for superconductivity (26) and whether the pairing is of triplet or singlet character. We find that the intensity of $\chi^s(q=0)$ is $\sim 1/5$ of the dominant IC peak when spin-orbit (SO) coupling is suppressed. But SO coupling lifts band degeneracies at

high symmetry points, reducing this ratio slightly to $\sim 1/7$. Thus χ^s seems to be dominated by fluctuations at the IC vector. Hence, such spin fluctuation spectra should favour pairing mainly in the spin singlet channel, absent other channels to provide extra glue for a triplet pairing. However, the continuum of spin excitation prevalent in most part of the Brillouin zone also can contribute to the glue.

As strain is applied $\text{Im}\chi^s(q, \omega)$ becomes sharper and more coherent, reaching a maximum coherence at $\epsilon_x = \epsilon_x^*$: the peak intensity remains at q^{IC} but nearly doubles in strength and shifts to slightly smaller ω . Also $\text{Im}\chi^s$ loses its two-dimensional character: the q_z dependence is significant and the dominant peak is most intense at $1/4$. For still larger ϵ_x , coherence begins to be lost. At $\epsilon_x = 1.2\%$ the IC peak $(0.3, 0.3, q_z)$ survives but χ^s becomes incoherent and diffused over a range q both in the plane and out of it, with another peak appearing near $(0.15, 0.15, 0)$. In short, for $\epsilon_x > \epsilon_x^*$, two prominent changes are observed: incommensurate but nearly ferromagnetic excitations at $(0.15, 0.15, 0)$ and commensurate gapped antiferromagnetic spin excitations at $(1/2, 1/2, a/2c)$.

Charge susceptibilities and commensurability: The evolution of the spin and charge susceptibilities are instructive to understand the changes in the gap symmetries under strain and their underlying even- or odd-parity characters. We find that the real part of the charge susceptibilities in the static limit $\chi^c(q, \omega \rightarrow 0)$, has strong peaks both at the nearly ferromagnetic $\sim (0.2, 0.2, 0)$ vector and also at more commensurate higher wavelength quasi-anti-ferromagnetic vector $(1/2, 1/2, 0)$ (Fig. 3). Raghu et al. discuss a possible route to superconductivity through charge fluctuations originating from the quasi one-dimensional bands d_{xz} and d_{yz} (35). Their analysis relies on the quasi one-dimensional character of these states.

Our *ab initio* calculation partially supports this picture. However, we also observe nearly comparable multi-orbital charge fluctuations, both intra and inter-orbital in nature, in all active bands (Fig 3). *Inter*-orbital charge fluctuations originating from d_{xz} and d_{yz} and the two-

dimensional d_{xy} are comparable to, or even larger than the intra-orbital contributions.

In the unstrained case, nearly uniform long-wavelength coherent charge fluctuations support a triplet pairing channel mainly through multi-orbital charge fluctuations. There is a significant peak in χ^q at small q , near $(0.2, 0.2, 0)$. However, there is another broad peak near $(1/2, 1/2, 0)$. Under strain, the latter peak becomes more coherent and larger, while the former decays. At the critical strain ϵ_x^* only the latter peak at $(\frac{1}{2}, \frac{1}{2}, 0)$ remains. Also χ^s and χ^c become increasingly coherent close to a vector that favors singlet pairing. This is strikingly different from the unstrained scenario where both spin and charge fluctuations have favourable triplet components as well. For $\epsilon_x > \epsilon_x^*$, the χ^c at $(\frac{1}{2}, \frac{1}{2}, 0)$ becomes large. Simultaneous shifts in spin fluctuation weight towards more commensurate lower q (larger wavelength) leaves $\chi^s(q^{\text{IC}})$ incoherent. This emergent incoherence in spin fluctuations at IC vector is not conducive for pairing.

Superconducting pairing: nodal character and dimensionality: The superconducting pairing susceptibility χ^{p-p} is computed by dressing the non-local pairing polarization bubble $\chi^{0,p-p}(\mathbf{k}, i\nu)$ with the pairing vertex $\Gamma^{irr,p-p}$ using the Bethe-Salpeter equation in the particle-particle channel.

$$\chi^{p-p} = \chi^{0,p-p} \cdot [\mathbf{1} + \Gamma^{irr,p-p} \cdot \chi^{0,p-p}]^{-1} \quad (3)$$

Where the non-local pairing vertex $\Gamma^{irr,p-p}$ in the singlet (s) and triplet (t) channels are obtained from the magnetic (spin) and density (charge) particle-hole reducible vertices by

$$\begin{aligned} \Gamma_{\alpha_1, \alpha_3}^{irr,p-p,s}(\mathbf{k}, i\nu, \mathbf{k}', i\nu') &= \Gamma_{\alpha_1, \alpha_3}^{f-irr}(\mathbf{k}, i\nu, \mathbf{k}', i\nu') + \frac{1}{2} \left[\frac{3}{2} \tilde{\Gamma}^{p-h,(m)} - \frac{1}{2} \tilde{\Gamma}^{p-h,(d)} \right]_{\alpha_1, \alpha_4}^{\alpha_2, \alpha_3}(\mathbf{k}, i\nu, \mathbf{k}', -i\nu')_{\mathbf{k}'-\mathbf{k}, i\nu'-i\nu} \\ &+ \frac{1}{2} \left[\frac{3}{2} \tilde{\Gamma}^{p-h,(m)} - \frac{1}{2} \tilde{\Gamma}^{p-h,(d)} \right]_{\alpha_1, \alpha_2}^{\alpha_4, \alpha_3}(\mathbf{k}, i\nu, \mathbf{k}', i\nu')_{-\mathbf{k}'-\mathbf{k}, -i\nu'-i\nu} \end{aligned} \quad (4)$$

$$\begin{aligned} \Gamma_{\alpha_1, \alpha_3}^{irr,p-p,t}(\mathbf{k}, i\nu, \mathbf{k}', i\nu') &= \Gamma_{\alpha_1, \alpha_3}^{f-irr}(\mathbf{k}, i\nu, \mathbf{k}', i\nu') - \frac{1}{2} \left[\frac{1}{2} \tilde{\Gamma}^{p-h,(m)} + \frac{1}{2} \tilde{\Gamma}^{p-h,(d)} \right]_{\alpha_1, \alpha_4}^{\alpha_2, \alpha_3}(\mathbf{k}, i\nu, \mathbf{k}', -i\nu')_{\mathbf{k}'-\mathbf{k}, i\nu'-i\nu} \\ &+ \frac{1}{2} \left[\frac{1}{2} \tilde{\Gamma}^{p-h,(m)} + \frac{1}{2} \tilde{\Gamma}^{p-h,(d)} \right]_{\alpha_1, \alpha_2}^{\alpha_4, \alpha_3}(\mathbf{k}, i\nu, \mathbf{k}', i\nu')_{-\mathbf{k}'-\mathbf{k}, -i\nu'-i\nu} \end{aligned} \quad (5)$$

Finally, χ^{p-p} can be represented as a function of eigenvalues λ and eigenfunctions ϕ^λ of the Hermitian particle-particle pairing matrix (see SM for the detailed derivation).

$$\chi^{p-p}(k, k') = \sum_{\lambda} \frac{1}{1-\lambda} \cdot (\sqrt{\chi^{0,p-p}(k)} \cdot \phi^\lambda(k)) \cdot (\sqrt{\chi^{0,p-p}(k')} \cdot \phi^\lambda(k')) \quad (6)$$

The pairing susceptibility diverges when the leading eigenvalue λ approaches one. The corresponding eigenfunction represents the momentum structure of χ^{p-p} . However, unlike hole doped cuprates or doped single-band Hubbard model (36), the unconventional superconductivity in SRO is multi-orbital in nature with a close packed eigenvalue spectrum, which warrants for more detailed investigation of the different eigenfunctions. These eigenfunctions are in different intra- and inter-orbital basis and not embedded into band representation to project the superconducting gap on the Fermi surfaces. To embed these normal phase momentum dependent pairing instabilities in orbital basis to band basis is needed further developments. Once this is done, we can gap out the Fermi surfaces by diagonalizing a Bogoliubov Hamiltonian built in the band basis (37).

As is apparent from Eqns. 4, 5 at what wave vector spin and charge fluctuations are strong is of central importance to the kind of superconducting pairing symmetry they can form. If superconductivity is driven by fluctuations near the ferromagnetic point (0,0,0), the spin part of the Cooper pair is symmetric and the superconductivity should have triplet symmetry. If, on the other hand if the fluctuations (spin or charge) are more proximate to $(1/2, 1/2, q_z)$, the symmetry is more likely to be singlet.

The nature of the candidate superconducting gap structures is strongly debated already in pristine SRO. Before turning to the strain dependence, we analyze in detail the gap structures that come out of QSGW+DMFT+BSE in both singlet and triplet channels. We further analyze how these different gap structures transform under spin exchange \hat{S} , orbital exchange \hat{O} , time exchange \hat{T} and parity \hat{P} operators. This allows us to characterize their irreducible represen-

$\Delta_{(\alpha_1, \alpha_2), (\alpha_3, \alpha_4)}$	\hat{S}	\hat{O}	\hat{T}	\hat{P}	pairing functions	irred repsn
$d_{(xy, xy), (xy, xy)}$	-1	1	1	1	$d_{x^2-y^2}$	B_{1g}
$d_{(xz, xz), (yz, yz)}$	-1	1	1	1	S^\pm	A_{1g}
$d_{(xz, xz), (yz, yz)}$	-1	1	1	1	$d_{x^2-y^2}$	B_{1g}
$d_{(xy, xy), (xy, xy)}$	1	1	-1	1	S^\pm	A_{1g}
$d_{(xz, xz), (yz, yz)}$	1	1	-1	1	S^\pm	A_{1g}
$d_{(xz, xz), (yz, yz)}$	1	1	-1	1	$d_{x^2-y^2}$	B_{1g}

Table 1: Characterization of different singlet and triplet gap instabilities in terms of D_{4h} irreducible representation. Also shown is how these different gap instabilities transform under spin exchange \hat{S} , orbital exchange \hat{O} , time exchange \hat{T} and parity \hat{P} operators.

tations (irreps) in terms of the D_{4h} , while noting that under uniaxial strain, the point group symmetry reduces to D_{2h} and properties of the 4-fold rotational symmetry no longer apply.

Singlet channel: we find three dominant eigenvalues that contribute to the superconducting gap instabilities. The corresponding eigenfunctions are shown in Fig. 4. They all change sign; thus the gap instabilities have nodes. For $\epsilon_x=0$ we find that all eigenvalues are degenerate within numerical precision. In the Ru- $d_{xy, xy}$ channel, the gap function is a d -wave, approximately $\cos k_x - \cos k_y$, with a D_{4h} - B_{1g} irreducible representation. The other two eigenfunctions are respectively $\cos k_x$ and $\cos k_y$ in the $d_{xz, xz}$ and $d_{yz, yz}$ channels. Hence, if a Cooper pair forms with two quasiparticles belonging to two different orbitals then it is possible to get an in-phase extended s -wave symmetry with a $d_{xz, yz}$ gap function $\cos k_x + \cos k_y$ with irreducible representation A_{1g} . However, it is also possible that Cooper pairs form with quasi-particles being out of phase, and hence, leading to a $d_{xz, yz}$ gap function with d -wave $\cos k_x - \cos k_y$ symmetry. Finally, all three eigenvalues increase as temperature drops (see SM), suggesting that SRO indeed has instabilities in the spin-singlet channel with nodes that could potentially drive Cooper pair formation. This provides a natural explanation for why nodal gap structures are reported from several measurements and previous theoretical studies based on model Hamiltonians (38, 39, 40, 41, 42, 43, 44). More importantly the new NMR data from Pustogow and

Luo et al. (45) and Ishida et al (46) have changed the course of discussion significantly in the lines of possible singlet instabilities in SRO from the usual triplet routes. Our study and observation of three singlet eigenvalues present in SRO is significant and timely. However, only recently has pure nodal line gap character been observed experimentally along the Cartesian z -direction (47). Owing to technical limitations the experiments by Hassinger et al. (47) cannot shed light on the character of the nodal gap structure in the basal plane, but they find strong evidence for nodal lines along q_z , making a case for the H_{c2} anomaly in SRO. In a very recent specific heat study, under angular variation of magnetic field at very low temperatures, Kittaka et al. (48) established the presence of horizontal line nodes in the gap structure. At this stage we can not shed light onto these observations as our analysis of gap instabilities are at present restricted analysis within an orbital basis, as perturbations from normal phase.

Triplet channel: A very different story emerges. We find nodeless gap functions as shown in Fig. 4. As in the singlet case, three eigenvalues are found. In the $d_{xz,xz}$ and $d_{yz,yz}$ channels we observe instabilities of the form $\delta_0 + \cos k_x$ and $\delta_0 + \cos k_y$, leading to the possibility of an extended nodeless s -wave $2\delta_0 + \cos k_x + \cos k_y$ gap structure with A_{1g} irreducible representation in the $d_{xz,yz}$ basis. The out of phase coupling between these two quasi-particles will lead to B_{1g} nodeless d -wave gap structure. We also observe an extended s -wave gap function in the $d_{xy,xy}$ channel. However, additionally we find a doubly-degenerate set of eigenvalues in an off-diagonal $d_{xz,xy}, d_{yz,xy}$ channel. Comparing singlet and triplet channels at fixed temperature, the triplet eigenvalues are nearly two times larger than singlet eigenvalues (see Fig. 4). For summary of all gap functions and their irreps see Table 1. In short, in the unstrained SRO, triplet channel dominates when it comes to Cooper pair formation, however, that does not exclude the possibility of formation of singlet Cooper pairs.

These calculations are performed in the normal phase of the SRO ($T > 1.5$ K), probing all possible particle-particle instabilities that could precipitate formation of a superconducting gap.

These solutions do not describe the superconducting state itself, and thus do not include possibility of spontaneously breaking time reversal symmetry (TRS). However, instabilities that do appear are candidates tailor-made for a complex order parameter prescribed in earlier theoretical works, notably by Raghu et al. (35), Scaffidi et al. (49) and Mackenzie et al. (6). Such an order parameter can result in a nodeless gap structure which can also lead to TRS breaking and chiral superconductivity. Also, two-component odd-frequency gap functions can lead to observed Kerr rotation (50) in SRO. We cannot draw conclusions on these works since at present our *ab initio* technique limited to discussion of the instabilities towards superconductivity. However, that the triplet eigenvalues being larger than the singlet ones in the pristine case strongly suggests triplet pairing dominates.

Remarkably, the roles reverse under strain. We find that the eigenvalues in the triplet channel decrease rapidly, while the singlet eigenvalues increase (see Fig. 4). At the critical strain $\epsilon_x = \epsilon_x^* = 0.6\%$ we observe that the singlet eigenvalues begin to overtake the triplet eigenvalues, suggesting a strong suppression of the triplet superconducting instability. Additionally, we find that the triplet eigenvalues are weakly dependent on temperature at this critical ϵ_x^* while the singlet eigenvalues start to diverge with lowering temperatures. This implies that the superconducting state switches from being dominated by triplet pairing at $\epsilon_x = 0$ to singlet pairing at $\epsilon_x = \epsilon_x^*$. This is fully consistent with the susceptibility calculations, which suggest that under strain both spin and charge fluctuations becomes more intense close to singlet vectors, and far from triplet $q = 0$.

Spin-charge co-operation in singlet channel under strain: To address the issue conclusively we compute the eigenvalues with and without the charge vertex functions. With both spin and charge vertex functions (as the calculations should be performed), we observe that for $\epsilon_x = 0$ triplet eigenvalues are larger than the singlet eigenvalues. On suppressing the charge vertex, we find that for $\epsilon_x = 0$, it does not have any effect on the result; triplet eigenvalues remain larger than

variants	λ_s^f	λ_t^f	λ_s^{-c}	λ_t^{-c}
$\epsilon_x=0$	0.006	0.011	0.005	0.014
$\epsilon_x > 0$	0.011	0.007	0.014	0.032

Table 2: The leading singlet and triplet eigenvalues computed using both spin and charge vertex functions λ_s^f, λ_t^f , and by suppressing the charge vertex functions $\lambda_s^{-c}, \lambda_t^{-c}$.

the singlet eigenvalues. However, for finite strain, $\epsilon_x > 0$, once the charge vertex is suppressed the triplet eigenvalues become larger than the singlet eigenvalues, which is in contrary to the observation including both spin and charge vertex functions. This is a strong indication that both spin and charge vertex functions co-operate under strain in the singlet channel. In Table 2 we show the eigenvalues with and without the charge vertex to make a case for this argument.

Conclusion: multiple singlet and triplet superconducting instabilities are observed in SRO. A purely spin triplet superconductivity needs sufficient coherent and low energy spin fluctuation glue near ferromagnetic vector $q=0$. However, our results show that the dominant spin fluctuations are at $(0.3, 0.3, q_z)$ which is closer to the singlet-pairing vector, combined with the smaller peak at the quasi-ferromagnetic ‘triplet’ vector. Multi-orbital charge correlations also play a central role in Sr_2RuO_4 : they provide additional glue both at low- q and $(0.5, 0.5, q_z)$ through strong intra- and inter-orbital fluctuations. Together, they lead to multiple triplet and singlet Cooper pair instabilities, although triplet eigenvalues are larger than the singlet eigenvalues.

When strain is applied the dominant character of Cooper pair instability changes. $\chi^s(q=0.3, 0.3, q_z)$ becomes more coherent up to a critical strain ϵ_x^* . Simultaneously the spectral weight under the low- q charge peak in gets fully transferred to a more coherent quasi-anti-ferromagnetic vector $(0.5, 0.5, q_z)$. Together they suggest, spin and charge co-operate to sustain an even parity pairing channel which maximize T_c at ϵ_x^* . For $\epsilon_x > \epsilon_x^*$, the spin fluctuation weight drifts toward larger wavelength, more uniform quasi-ferromagnetic vectors and charge fluctuates more strongly at the quasi-anti-ferromagnetic vector. This emergent spin incoherence and spin-charge separa-

tion, split by quasi-ferromagnetic spin fluctuation peak and quasi-anti-ferromagnetic charge fluctuation peak, is not conducive for sustaining the even-parity superconductivity and hence lowers and suppresses T_c . Our observations suggest that the pathway to maximize superconductivity in Sr_2RuO_4 would be to cause spin and charge fluctuations to act in symphony in an even parity channel.

Acknowledgments

Authors acknowledge F. Baumberger for sharing with us the raw ARPES data for Fermi surfaces. SA acknowledges discussions with James Annett, Martin Gradhand and Astrid Romer. This work was supported by the Simons Many-Electron Collaboration, and EPSRC (grants EP/M011631/1 and EP/M011038/1). For computational resources, we were supported by the ARCHER UK National Supercomputing Service, UK Materials and Molecular Modelling Hub for computational resources, (EPSRC grant EP/P020194/1) and computing resources provided STFC Scientific Computing Department’s SCARF cluster and PRACE supercomputing facility.

Method

We use a recently developed quasi-particle self consistent GW + dynamical mean field theory (QSGW+DMFT) (21, 22), as implemented in the all-electron Questaal package (25). Paramagnetic DMFT is combined with nonmagnetic QSGW via local projectors of the Ru $4d$ states on the Ru augmentation spheres to form the correlated subspace. We carried out the QSGW calculations in the tetragonal and strained phases of Sr_2RuO_4 with space group 139/I4mmm. DMFT provides a non-perturbative treatment of the local spin and charge fluctuations. We use an exact hybridization expansion solver, namely the continuous time Monte Carlo (CTQMC) (51), to solve the Anderson impurity problem.

The one-body part of QSGW is performed on a $16 \times 16 \times 16$ k-mesh and charge has been converged up to 10^{-6} accuracy, while the (relatively smooth) many-body static self-energy $\Sigma^0(\mathbf{k})$ is constructed on a $8 \times 8 \times 8$ k-mesh from the dynamical GW $\Sigma(\mathbf{k}, \omega)$. $\Sigma^0(\mathbf{k})$ is iterated until convergence (RMS change in $\Sigma^0 < 10^{-5}$ Ry). $U=4.5$ eV and $J=1.0$ eV (52) were used as correlation parameters for DMFT. The DMFT for the dynamical self energy is iterated, and converges in ≈ 20 iterations. Calculations for the single particle response functions are performed with 10^9 QMC steps per core and the statistics is averaged over 64 cores. The two particle Green's functions are sampled over a larger number of cores (40000-50000) to improve the statistical error bars. We sample the local two-particle Green's functions with CTQMC for all the correlated orbitals and compute the local polarization bubble to solve the inverse Bethe-Salpeter equation (BSE) for the local irreducible vertex. Finally, we compute the non-local polarization bubble $G(\mathbf{k}, \omega)G(\mathbf{k}-\mathbf{Q}, \omega-\Omega)$ and combined with the local irreducible vertex (33) we obtain the full non-local spin and charge susceptibilities $\chi^{s,c}(\mathbf{Q}, \Omega)$. The susceptibilities are computed on a $16 \times 16 \times 16$ Q-mesh. BSE equations in the particle-particle pairing channels are solved on the same k-mesh to extract the susceptibilities and the Eliashberg eigenvalue equations are solved to extract the eigenvalue spectrum and corresponding pairing symmetries (36).

Author contributions

SA has conceived and designed the research. SA, MvS have carried out the calculations. SA, DP, HP, MvS have contributed codes. DP, MvS have prepared the figures. All authors have contributed to the writing of the paper and the analysis of the data.

Additional information

Supplementary material is available.

Competing financial interests

The authors declare no competing financial interests.

Correspondence

All correspondence, code and data requests should be made to SA.

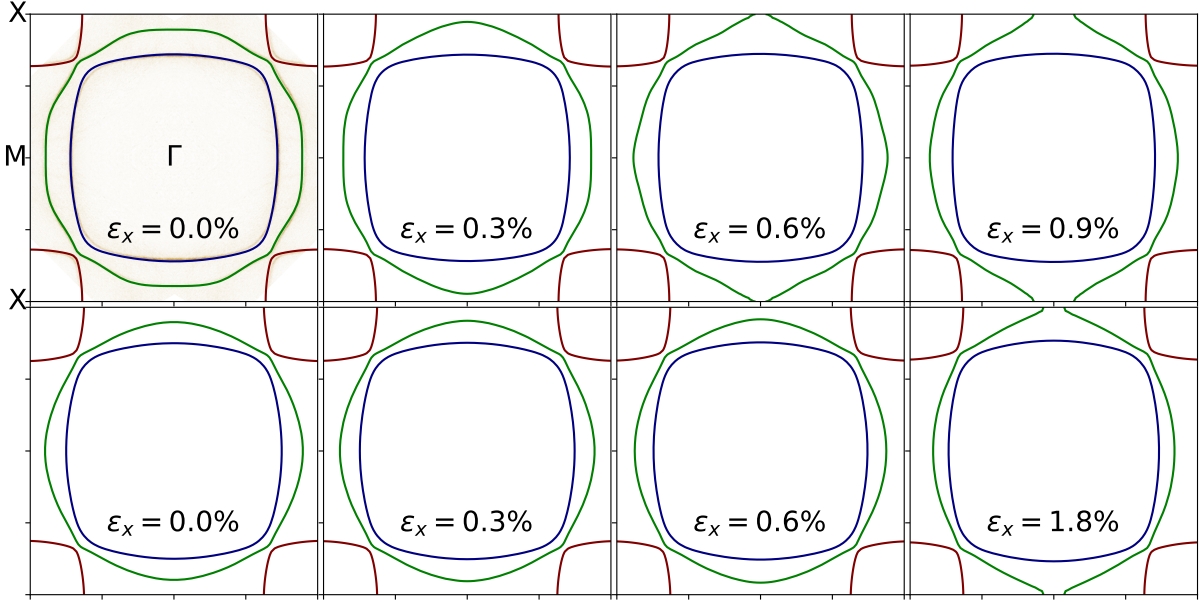


Figure 1: **Evolution of Fermi surface topology under strain:** Top row shows the QSGW Fermi surfaces in the basal plane, for a [100] compressive strain with $\epsilon_x=(0\%, 0.3\%, 0.6\%, 0.9\%)$. Spin orbit coupling is included (its omission makes a modest change to the Fermi surfaces). In the first panel (top left) high-resolution ARPES data (28) (figure is replotted using the raw ARPES data) for the Fermi surfaces are shown (figure reproduced with due permission) in the background of our QSGW theoretical data. For a higher resolution comparison please see the SM. States derive almost exclusively of Ru t_{2g} orbitals xy, xz, yz ; the orbital character of each pocket changes moving around the contour. xy character is present on the entire Fermi surface: it resides on the blue pocket on the Γ -X line, and on the green on the Γ -M line. Under strain, the four M points lose the 4-fold rotational symmetry, and at $\epsilon_x = \epsilon_x^*$ the topology of the green band changes. Bottom row shows corresponding results for DFT. In DFT the transition also occurs, but near $\epsilon_x=1.8\%$ (bottom right panel), instead of ϵ_x^* .

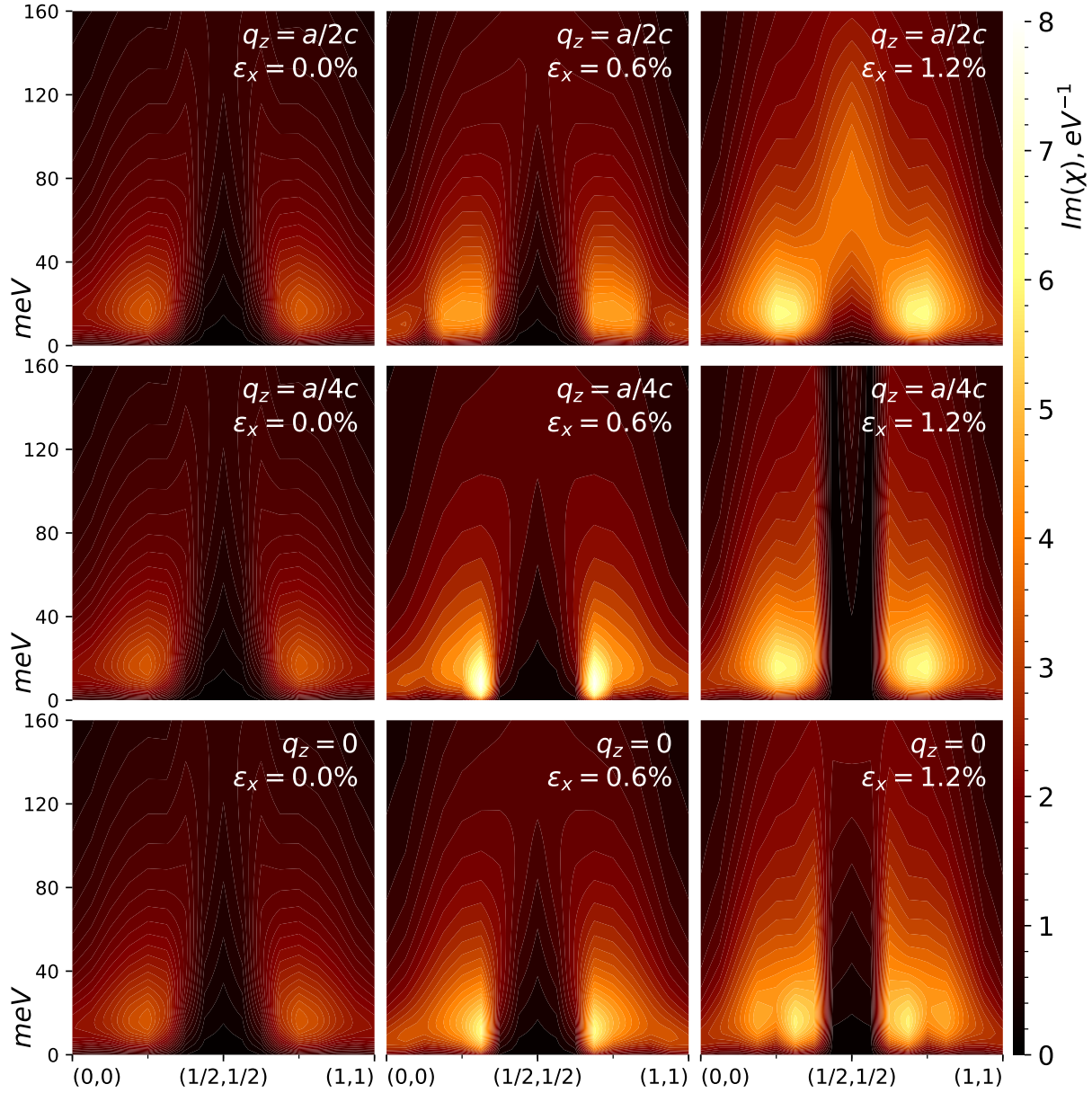


Figure 2: **Spin fluctuations: incommensurability and coherence:** Imaginary part of the dynamic spin susceptibility $\chi^s(q, \omega)$ are shown in the Cartesian xy plane at different values q_z , and for different strains ϵ_x . The unstrained compound shows a spin fluctuation spectrum strongly peaked at $(0.3, 0.3, q_z)$ (units $2\pi/a$). At $\epsilon_x=0$, χ^s is nearly independent of q_z , but it begins to depend on q_z for $\epsilon_x>0$. With increasing strain fluctuations become more coherent and strongly peaked, reaching a zenith at $\epsilon_x=\epsilon_x^*$ (0.6%), where T_c is maximum. For $\epsilon_x>\epsilon_x^*$, this peak becomes more diffuse; also a secondary incoherent peak emerges at $(0.15, 0.15, q_z)$, and the quasi anti-ferromagnetic vector $(1/2, 1/2, a/2c)$ acquires spectral weight around $\omega=40$ meV. Note also the spectral weight near the FM vector $(0,0,0)$, and its evolution with ϵ_x .

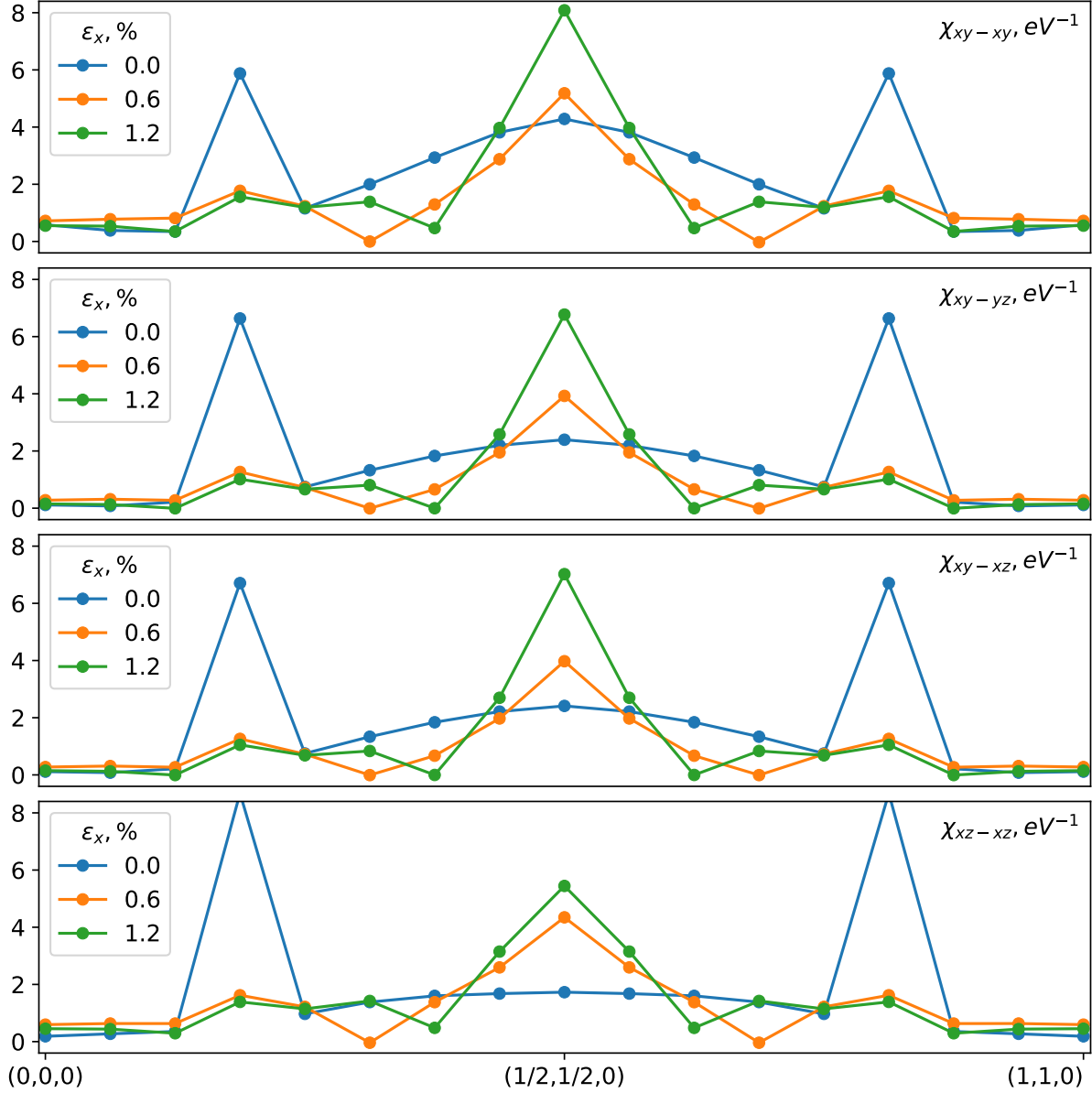


Figure 3: **Charge susceptibilities and commensurability:** Real part of the static charge susceptibility $\chi^c(q, \omega = 0)$, shown along the Cartesian (000) to (110) direction, and for different strains ϵ_x . The unstrained compound shows three-peaked charge fluctuation, with sharp peaks at IC vector (0.2, 0.2, 0) (and by symmetry at (0.8, 0.8, 0)) and a broad peak at (0.5, 0.5, 0). With strain the structure becomes sharply single-peaked at commensurate (0.5, 0.5, 0). The peak at the commensurate vector develops at the cost of the charge fluctuation weights from the IC vectors. The systematic evolution from large wavelength triplet to shorter wavelength singlet fluctuations, under strain, is common to all inter- and intra-orbital charge fluctuations. The strong, often the most dominant, inter-orbital charge fluctuations can be observed in Ru- d_{xy-xz} and Ru- $d_{xy,yz}$ channels.

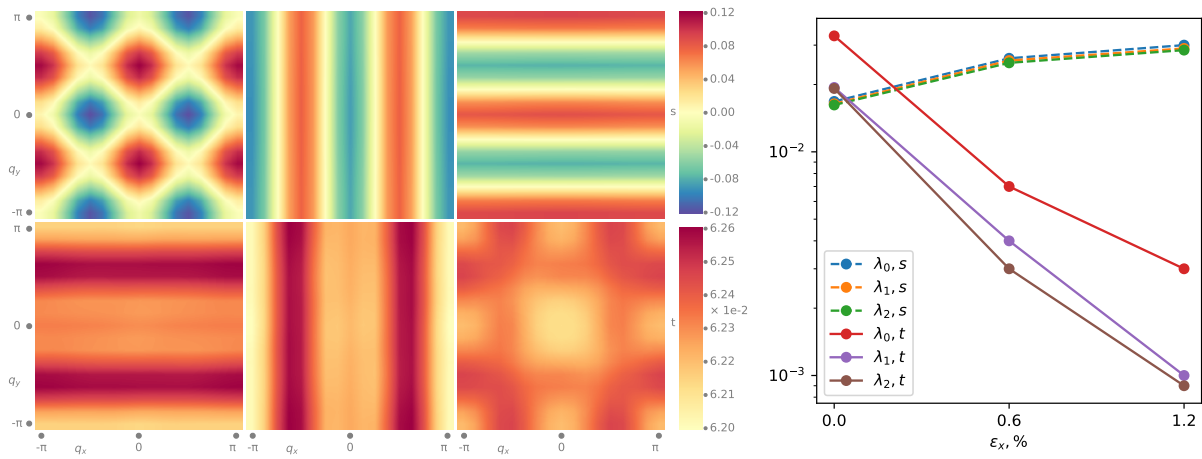


Figure 4: **Superconducting pairing: nodal character:** (left panel) The superconducting pairing gap symmetries for $\epsilon_x=0$ are shown in the (100)-(010) plane; eigenfunctions corresponding to first three eigenvalues in singlet (s) symmetries are in the top panel and triplets (t) are in the lower panel . Right panel shows evolution of triplet and singlet eigenvalues under strain. Under strain singlet eigenvalues increase and surpass the triplet eigenvalues.

References

1. H. Onnes, *Commun. Phys. Lab. Univ. Leiden* (1911).
2. L. N. Cooper, *Phys. Rev.* **104**, 1189 (1956).
3. A. Mackenzie, *et al.*, *Physical review letters* **80**, 161 (1998).
4. C. Nayak, S. H. Simon, A. Stern, M. Freedman, S. D. Sarma, *Reviews of Modern Physics* **80**, 1083 (2008).
5. Y. Maeno, *et al.*, *Nature* **372**, 532 (1994).
6. A. P. Mackenzie, T. Scaffidi, C. W. Hicks, Y. Maeno, *npj Quantum Materials* **2**, 40 (2017).
7. Y. Maeno, *et al.*, *Physical review letters* **81**, 3765 (1998).
8. S. Kittaka, T. Nakamura, H. Yaguchi, S. Yonezawa, Y. Maeno, *Journal of the Physical Society of Japan* **78**, 064703 (2009).
9. Y. Ying, *et al.*, *Physical review letters* **103**, 247004 (2009).
10. C. W. Hicks, *et al.*, *Science* **344**, 283 (2014).
11. A. Steppke, *et al.*, *Science* **355**, eaaf9398 (2017).
12. Y. Imai, M. Sigrist, *Physica B: Condensed Matter* **536**, 72 (2018).
13. Y.-C. Liu, F.-C. Zhang, T. M. Rice, Q.-H. Wang, *npj Quantum Materials* **2**, 12 (2017).
14. M. E. Barber, A. S. Gibbs, Y. Maeno, A. P. Mackenzie, C. W. Hicks, *Physical review letters* **120**, 076602 (2018).
15. J. Mravlje, *et al.*, *Physical review letters* **106**, 096401 (2011).

16. C. Veenstra, *et al.*, *Physical review letters* **112**, 127002 (2014).
17. S. Acharya, M. S. Laad, D. Dey, T. Maitra, A. Taraphder, *Scientific Reports* **7**, 43033 (2017).
18. L. Boehnke, P. Werner, F. Lechermann, *arXiv preprint [arXiv:1806.01511](https://arxiv.org/abs/1806.01511)* (2018).
19. G. Baskaran, *Physica B: Condensed Matter* **223**, 490 (1996).
20. S. Acharya, D. Dey, T. Maitra, A. Taraphder, *Journal of Physics Communications* (2018).
21. S. Acharya, *et al.*, *Phys. Rev. X* **8**, 021038 (2018).
22. L. Sponza, *et al.*, *Physical Review B* **95**, 041112 (2017).
23. J. M. Tomczak, M. van Schilfgaarde, G. Kotliar, *Phys. Rev. Lett.* **109**, 237010 (2012).
24. D. Pashov, *et al.*, *arXiv preprint [1907.06021](https://arxiv.org/abs/1907.06021)* (2019).
25. Questaal website, <https://www.questaal.org>. Our *GW* implementation was adapted from the original ecalj package, now at <https://github.com/tkotani/ecalj/>.
26. P. Steffens, *et al.*, *arXiv preprint [arXiv:1808.05855](https://arxiv.org/abs/1808.05855)* (2018).
27. C. Bergemann, A. Mackenzie, S. Julian, D. Forsythe, E. Ohmichi, *advances in Physics* **52**, 639 (2003).
28. A. Tamai, *et al.*, *Phys. Rev. X* **9**, 021048 (2019).
29. S. Liu, *et al.*, *Physical Review B* **86**, 165112 (2012).
30. M. Braden, *et al.*, *Physical Review B* **66**, 064522 (2002).

31. M. Braden, *et al.*, *Physical review letters* **88**, 197002 (2002).
32. K. Ishida, *et al.*, *Physical Review B* **63**, 060507 (2001).
33. H. Park, K. Haule, G. Kotliar, *Phys Rev Lett.* **107**, 137007 (2011).
34. K. Iida, *et al.*, *Physical Review B* **84**, 060402 (2011).
35. S. Raghu, A. Kapitulnik, S. Kivelson, *Physical review letters* **105**, 136401 (2010).
36. H. Park, The study of two-particle response functions in strongly correlated electron systems within the dynamical mean field theory, Ph.D. thesis, Rutgers University-Graduate School-New Brunswick (2011).
37. Z. Yin, K. Haule, G. Kotliar, *Nature Physics* **10**, 845 (2014).
38. L.-D. Zhang, W. Huang, F. Yang, H. Yao, *Physical Review B* **97**, 060510 (2018).
39. I. Eremin, D. Manske, S. Ovchinnikov, J. Annett, *Annalen der Physik* **13**, 149 (2004).
40. G. Litak, J. Annett, B. Györfly, K. Wysokiński, *physica status solidi (b)* **241**, 983 (2004).
41. P. Contreras, M. Walker, K. Samokhin, *Physical Review B* **70**, 184528 (2004).
42. K. Ishida, *et al.*, *Phys. Rev. Lett.* **84**, 5387 (2000).
43. M. Zhitomirsky, T. Rice, *Physical review letters* **87**, 057001 (2001).
44. P. Contreras, M. Walker, K. Samokhin, *Physical Review B* **70**, 184528 (2004).
45. A. Pustogow, *et al.*, *arXiv preprint* [arXiv:1904.00047](https://arxiv.org/abs/1904.00047) (2019).
46. K. Ishida, M. Manago, Y. Maeno, *arXiv preprint* [arXiv:1907.12236](https://arxiv.org/abs/1907.12236) (2019).
47. E. Hassinger, *et al.*, *Physical Review X* **7**, 011032 (2017).

48. S. Kittaka, *et al.*, *Journal of the Physical Society of Japan* **87**, 093703 (2018).
49. T. Scaffidi, J. C. Romers, S. H. Simon, *Phys. Rev. B* **89**, 220510 (2014).
50. L. Komendová, A. M. Black-Schaffer, *Phys. Rev. Lett.* **119**, 087001 (2017).
51. K. Haule, G. Kotliar, *Phys. Rev. B* **76**, 104509 (2007).
52. X. Deng, K. Haule, G. Kotliar, *Physical Review Letters* **116** (2016).
53. Q. Huang, *et al.*, *Journal of Solid State Chemistry* **112**, 355 (1994)

1 Supplemental Material

In the supplementary material for our main paper titled ‘Evening out the spin and charge parity to increase T_c in unconventional superconductors’, we discuss structural inputs for our calculations, the non-trivial properties of SRO density of states (DOS), the relative orientations of QSGW energy levels, method for computation of superconducting gap structure and the importance of non-local electronic correlations in SRO. These discussions are beyond the limited scope of the main text, while help in understanding the technical details of our implementations and their relevance in understanding the physics discussed in the main paper.

Sr_2RuO_4 has a BCT lattice structure. We took the lattice parameters and internal positions from (53). The lattice constant in the basal plane is $a=3.86448 \text{ \AA}$. The uniaxial strain was performed at constant volume.

Local density of states (DOS): The DOS obtained from QSGW shows the presence of a sharp resonance slightly above the Fermi level in the unstrained case (Fig. 5). Strain splits the single peak, the splitting increasing linearly with ϵ_x . The smaller, lower peak crosses E_F at $\epsilon_x=0.6\%$, which precisely coincides with the critical strain ϵ_x^* where $T_C = T_C^{\max}$.

Energy levels: Strain lifts the tetragonal symmetry, splitting the degeneracy of the Ru ($4d_{xz}, 4d_{yz}$) and O (p_x, p_y) pairs. We find that the states split beyond the typical exchange scale of ~ 4 meV (Fig. 6) when $\epsilon_x=0.6\%$. The split between Ru $4d_{xz}, 4d_{yz}$ is extremely small, and might fall below the resolution of several measurements trying to probe directly the consequences of lifting of the native tetragonal symmetry under strain. However, O p_x, p_y states split by nearly 20-25 meV.

Non-local Coulomb correlations: As Coulomb interactions are long-range, they are treated by QSGW perturbatively in a self-consistent manner through a dynamic and momentum dependent self-energy, $\Sigma(\mathbf{k}, \omega)$. We analyse $\Sigma(\mathbf{k}, \omega)$ computed within QSGW to extract the momentum-dependent quasi-particle renormalization factor $Z_k = (1 - \partial\Sigma(\mathbf{k}, \omega)/\partial\omega)^{-1}$. Fig. 7 shows how the non-local $\Sigma(\mathbf{k}, \omega)$ renormalizes bands differently on the Γ -M line. The variation is orbital-dependent, fluctuating by $\sim 40\%$ in a nontrivial manner with \mathbf{k} , ω , and strain. This has a significant effect on the d bandwidth, and is one important reason why QSGW bands are significantly narrower than their LDA counterparts. Bandwidths are nevertheless much larger than ARPES measurements, and they get further renormalized by strong spin fluctuations included in DMFT.

Magnetic, charge and Superconducting susceptibilities: Here we show the Feynman diagram representation of the Bethe-Salpeter equation in the particle-hole (p-h) channel 8.

In order to extract Γ_{loc}^{irr} , we employ the Bethe-Salpeter equation which relates the local two-particle Green's function (χ_{loc}) sampled by CTQMC, with both the local polarization function (χ_{loc}^0) and Γ_{loc}^{irr} .

$$\Gamma_{loc}^{irr, m(d)}_{\alpha_1, \alpha_2, \alpha_3, \alpha_4}(i\nu, i\nu')_{i\omega} = [(\chi_{loc}^0)_{i\omega}^{-1} - \chi_{loc}^{m(d)-1}]_{\alpha_1, \alpha_2, \alpha_3, \alpha_4}(i\nu, i\nu')_{i\omega}. \quad (7)$$

The non-local polarization bubble in the p-h channel is computed from

$$\chi_{\alpha_3\sigma_3,\alpha_4\sigma_4}^0{}_{\alpha_1\sigma_1,\alpha_2\sigma_2}(i\nu, i\nu')_{\mathbf{q},i\omega} = -\frac{T}{N_k} \sum_{\mathbf{k}} G_{\alpha_2\alpha_1,\sigma_1}(\mathbf{k}, i\nu) \cdot G_{\alpha_3\alpha_4,\sigma_3}(\mathbf{k} + \mathbf{q}, i\nu + i\omega) \cdot \delta_{i\nu,i\nu'} \cdot \delta_{\sigma_1\sigma_2} \cdot \delta_{\sigma_3\sigma_4} \quad (8)$$

With these two quantities we can get the full dynamic and non-local spin and charge susceptibilities.

Further, we show the Feynman diagram representation of the p-p vertex and its decomposition using the p-h vertex function computed in the magnetic and density channels.

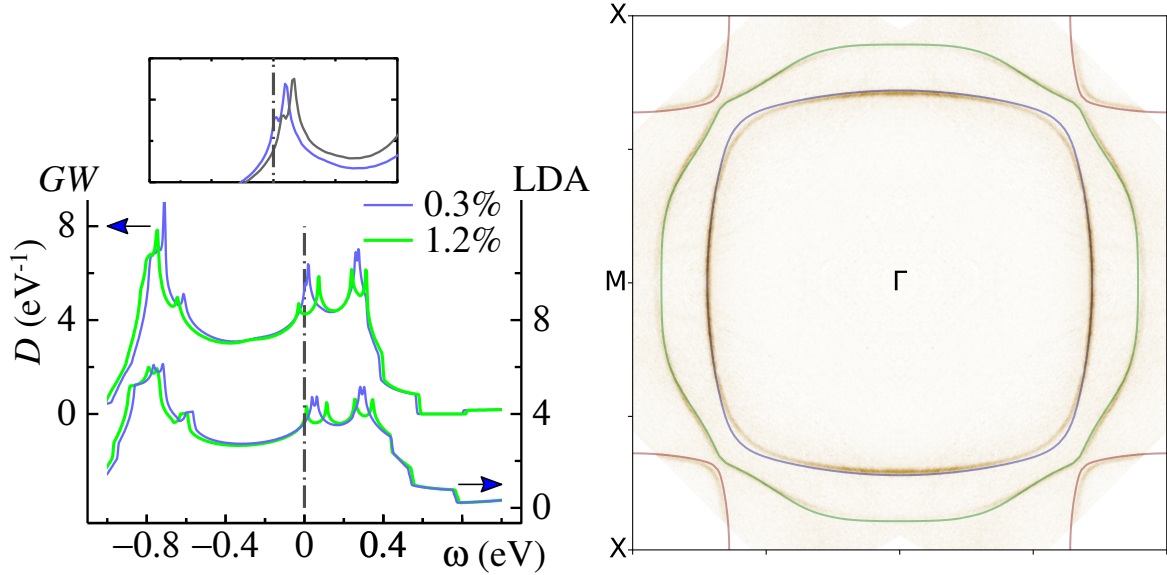


Figure 5: **Density of States:** Top pair of curves show density of states (DOS) from QSGW, for strains $\epsilon_x = 0.3\%$ (blue) and 1.2% (green). A Van-Hove singularity appears slightly above the Fermi level when $\epsilon_x=0$. When $\epsilon_x \neq 0$ the singularity splits into two peaks, with the smaller peak crossing E_F at $\epsilon_x=0.6\%$. An intriguing possibility is to find conditions that cause the larger peak to cross E_F . Bottom pair is the corresponding DOS in the LDA. The Van-Hove singularity and its splitting are also seen, but the peaks split more symmetrically, and evolve more slowly with ϵ_x . On average, the LDA DOS is 25% smaller than the QSGW DOS, which is a consequence of the LDA's tendency to overestimate d bandwidths. Inset shows the QSGW DOS at $\epsilon_x=0.3\%$ on finer energy scale. The grey line shows the DOS with spin-orbit coupling removed. To the right, the high-resolution ARPES data (28) for the Fermi surfaces are shown (figure reproduced with due permission) in the background of our QSGW theoretical data. Weak discrepancies can be observed for the quasi-one-dimensional Fermi sheets.

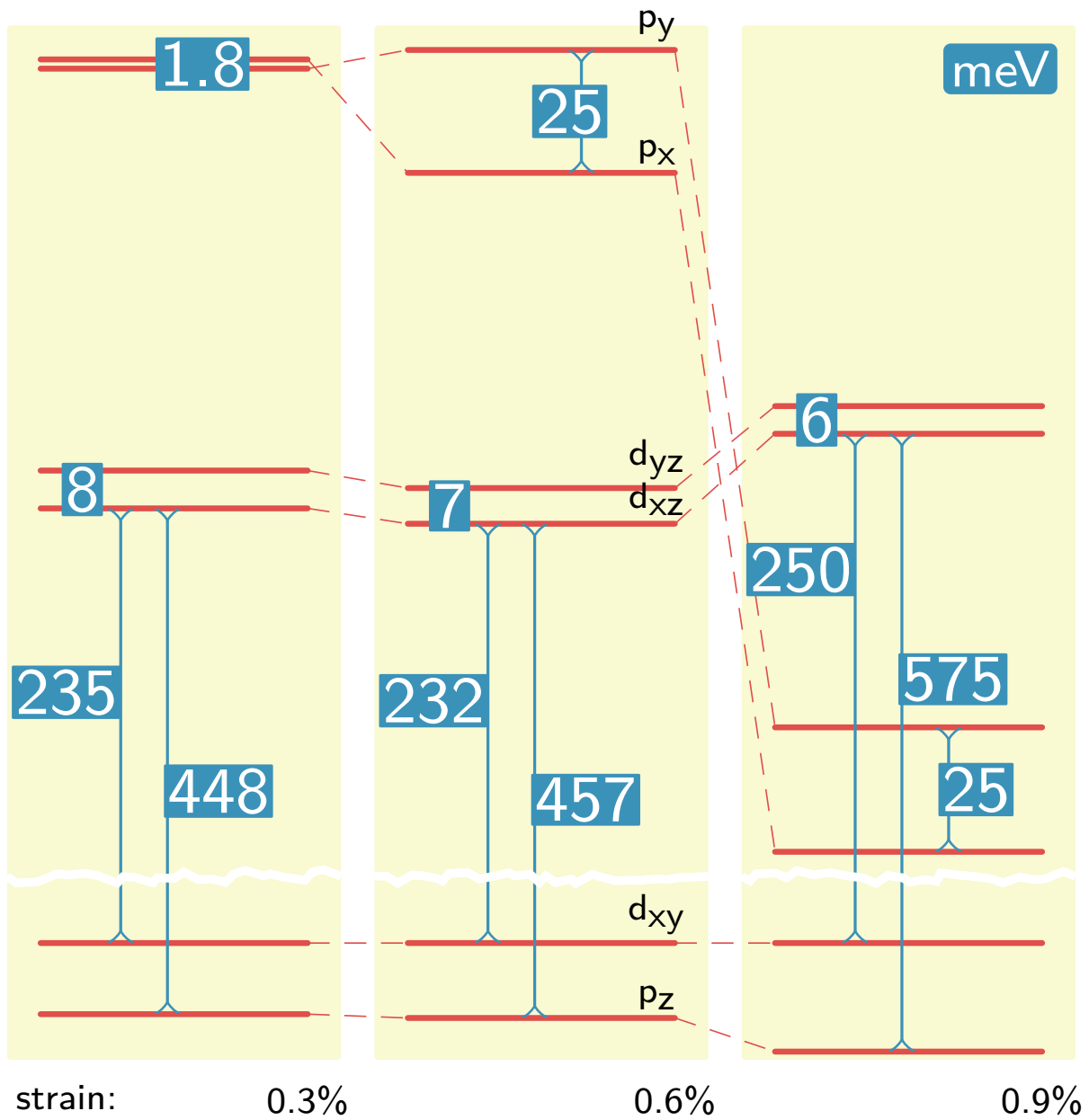


Figure 6: **Energy levels:** Relative orientations of different active orbitals in Sr_2RuO_4 from QSGW. In strained Sr_2RuO_4 , we find typical splitting of 6-8 meV between Ru- d_{xz} and d_{yz} orbitals and about 25 meV between O- p_x and O- p_y . This energy splitting is larger than the spin exchange scale in Sr_2RuO_4 .

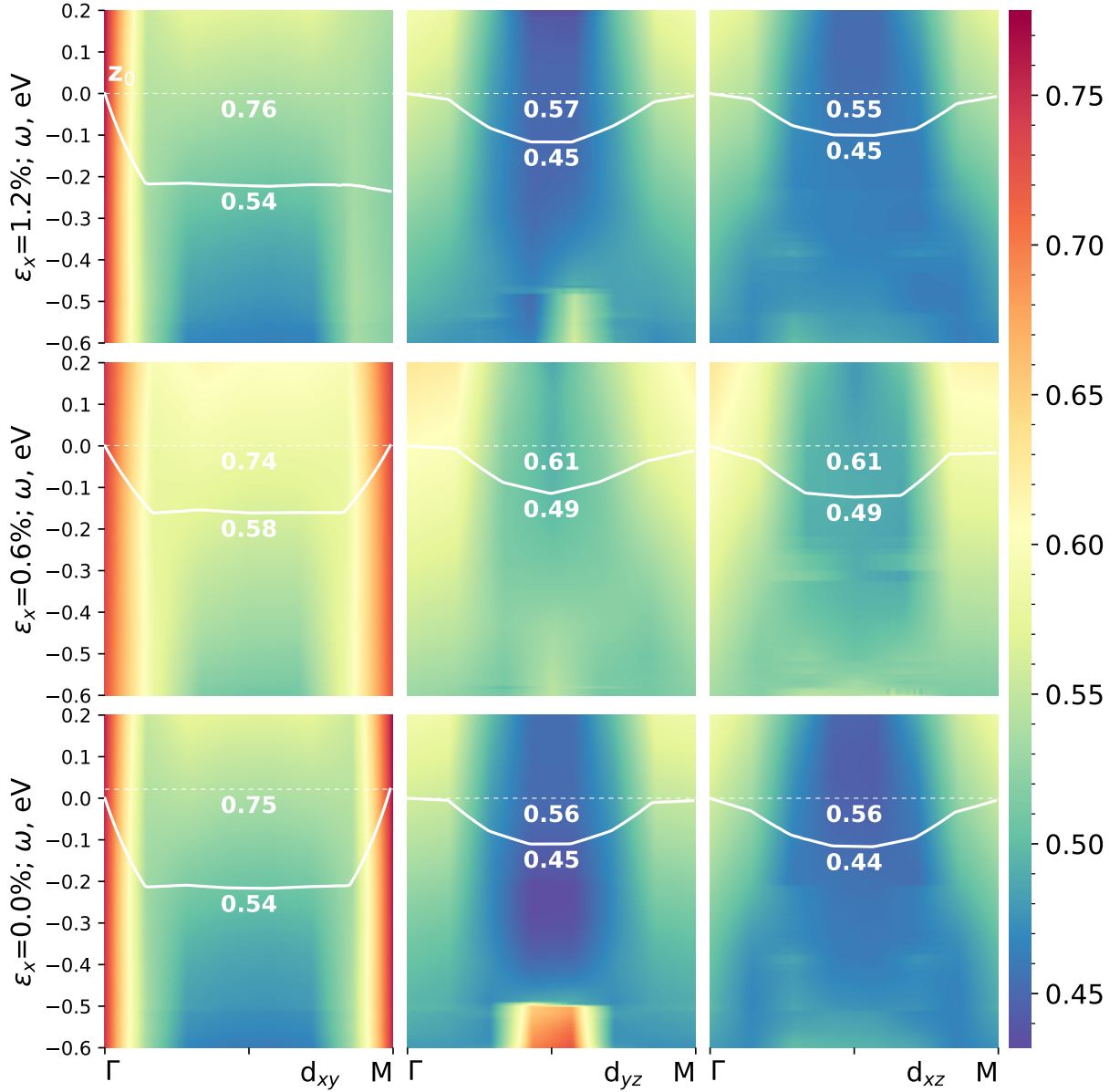


Figure 7: **Non-local correlations:** Quasi-particle renormalization factor, $Z_k(\omega)$, computed in QSGW, as a heat map in the k - ω plane. White lines detail Z at the Fermi energy ($\omega = 0$) along the Γ -M line. The three bands present at E_F are all of Ru t_{2g} character, respectively d_{xy} , d_{yz} , d_{xz} -like on this line (from left to right). Z is a measure of how strongly nonlocality in space and time renormalize and smear out the energy bands: at $Z=1$ electrons are perfectly coherent and act like independent particles; when $Z=0$ all coherence is lost. Its k -dependence is unusually strong. To put it in perspective, in iso-structural La_2CuO_4 , Z varies by $\sim 20\%$ (21) for the Cu- $d_{x^2-y^2}$ band. Lower panels show Z_k evolves in a non-trivial, orbital-dependent fashion with strain. Spin fluctuations missing in QSGW further reduce Z .

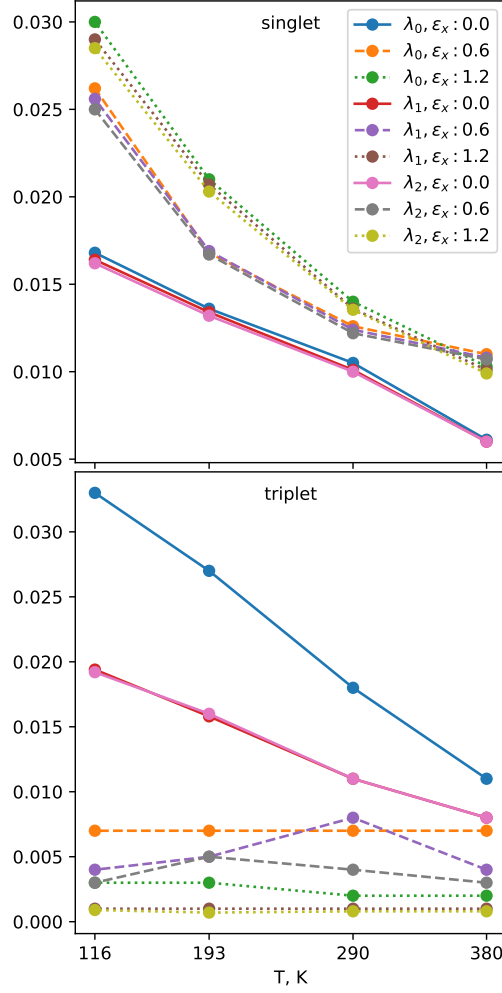
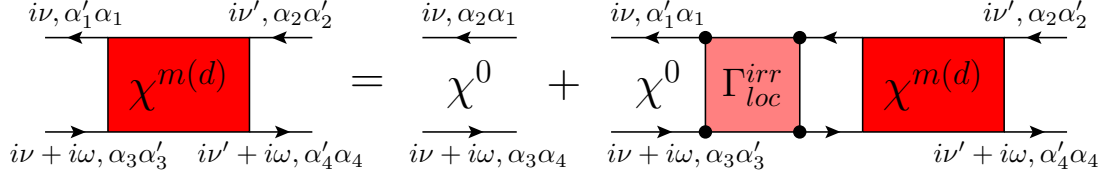


Figure 8: The Feynman diagram for the Bethe-Salpeter equation in the spin (charge) channel. The non-local susceptibility is obtained by replacing the local propagator by the non-local propagator. In lower panel first (λ_0), second (λ_1) and third (λ_2) eigenvalues with and without strain as function of temperature in singlet and triplet channels are shown.

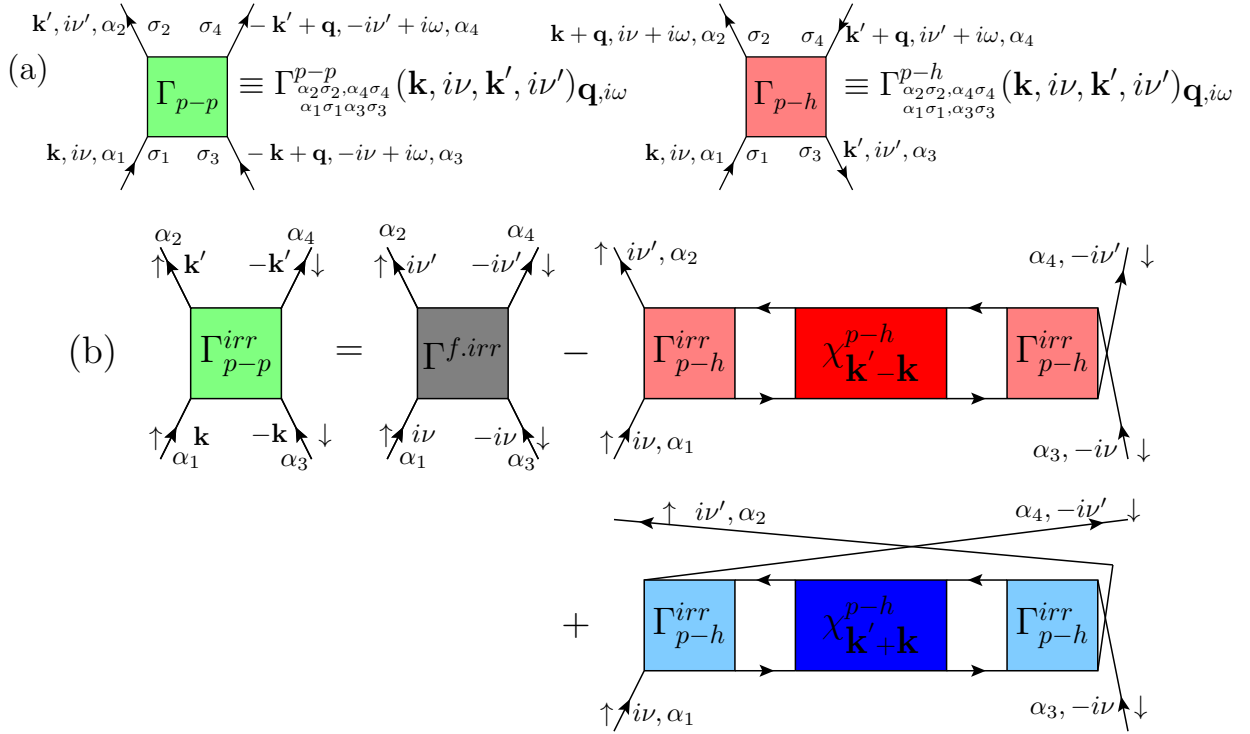


Figure 9: (a) The spin, orbital, momentum, and frequency labels of vertex functions in the particle-particle ($p - p$) channel and the particle-hole ($p - h$) channel. (b) The decomposition of the irreducible vertex function in the particle-particle channel $\Gamma^{irr,p-p}$.